

Optical layout of a beamline for photoemission microscopy

Th. Schmidt,^a J. Slezak,^a S. Heun,^a J. Diaz,^a R. R. Blyth,^a R. Delaunay,^a
D. Cocco,^a K. C. Prince,^{a*} E. Bauer^b and M. Coreno^c

^a*Sincrotrone Trieste, km 163.5, SS 14, Area Science Park, Basovizza, Trieste, Italy,*

^b*Department of Physics and Astronomy, Arizona State University, Tempe, AZ 85287-1504, USA, and* ^c*CNR-Istituto di Metodologie Avanzate Inorganiche, Montelibretti, I-00016 Rome, Italy. E-mail: kevin.prince@elettra.trieste.it*

(Received 29 September 1998; accepted 14 June 1999)

An optical layout for performing photoemission microscopy using synchrotron light from the storage ring Elettra is described. The microscope, property of the Technical University of Clausthal, was installed on an existing monochromator and the light is deflected and focused by two toroidal mirrors. A light spot of ~ 30 μm diameter and a photon energy range from 45 to 160 eV has been achieved. The light illuminates the sample in the microscope at grazing incidence and chemical contrast is observed in photoemission. Apart from the standard photoemission mode of operation with synchrotron radiation, surface NEXAFS spectra from microspot areas can be measured, and an example is shown. Images can also be obtained with variable kinetic energies (and therefore variable surface sensitivity) of the secondary electrons while working in NEXAFS mode. The obliquely incident soft X-rays cause shadows due to topography on the surface, which allows an estimate of the height of features. Three-dimensional islands give rise to Fresnel diffraction and many fringes may be visible. This effect and its consequences for chemical imaging are discussed.

Keywords: photoemission microscopy; beamlines; Fresnel diffraction.

1. Introduction

In this paper we describe the instrumentation used to install the SPELEEM (spectroscopic photoemission and low-energy electron microscope) at the synchrotron light source Elettra, and some preliminary results. The design of the soft X-ray beam transport optics was dictated by a number of constraints and we describe the solution adopted and the performance achieved.

An interesting result is connected with the phenomenon of Fresnel diffraction at an edge, which is a well known effect on both macroscopic and microscopic scales. It is manifested as a series of fringes whose intensity is damped with distance from the edge. Occasionally it has been observed in unexpected situations, *e.g.* when using hard X-rays incident at very grazing angles on a small mirror and reflected over large distances (Ferrer *et al.*, 1995). While investigating the growth of thin films by means of photoemission microscopy, we have encountered this phenomenon in a nanoscale system, namely lead islands on Si obliquely illuminated by soft X-rays. The edges of the islands are sharp and create diffraction patterns beside their shadows.

2. Experimental

The SPELEEM microscope of the Technical University of Clausthal (Veneklasen, 1991) was installed on a branch of

the gas-phase photoemission beamline, as described below. The spatial resolution has been measured to be better than 22 nm in photoemission, while 8 nm has been achieved with low-energy electron microscopy (LEEM) (Schmidt *et al.*, 1998). Secondary electrons or photoelectrons from the surface are accelerated to 18 keV, and pass through the electron microscope column and energy analyser, are amplified by a channel plate and strike a fluorescent screen to produce an image, which is acquired by a CCD camera. This is a unique instrument as no other microscope of this kind is installed at a synchrotron light source, and no other photoemission microscope with energy analysis has the facility to perform LEEM.

The sample described below was prepared by flashing an Si(111) wafer to remove the oxide thermally, and then held at ~ 500 K during metal deposition. Silver was evaporated from a crucible and formed a ($\sqrt{3} \times \sqrt{3}$) R30° structure, onto which lead was evaporated to form three-dimensional islands, after completion of the first layer (Stranski–Krastanov growth).

The source of soft X-rays is a 36-period undulator, and the beamline delivers high-intensity synchrotron light in the energy range 45–160 eV to the microscope. The *p*-polarized light is incident at a grazing angle of 15° onto the surface of the sample. The degree of linear polarization has been measured at high energy and is >99%.

The optical layout of the monochromator (Melpignano *et al.*, 1995) and the first results regarding performance

Table 1
Optical parameters of the deflection mirror and refocusing mirror.

Deflection mirror	
Major radius	13000 mm
Minor radius	150.1 mm
Angle of incidence of light	84°
Entrance arm	880 mm
Exit arm: horizontal/vertical	2980 mm/3890 mm
Magnification: horizontal/vertical	3.4/4.4
Substrate material	Zerodur
Coating	Gold
Refocusing mirror	
Major radius	3824.6 mm
Minor radius	29.05 mm
Angle of incidence of light	85
Entrance arm: horizontal/vertical	1320 mm/1410 mm
Exit arm	200 mm
Magnification	0.2
Substrate material	Zerodur
Coating	Gold

(Prince *et al.*, 1998) have been discussed elsewhere, but the optics of the branch beamline have not been described previously. The monochromator is constructed for high-energy resolving power (greater than 10000), and our design problem was to insert the microscope after the exit slit with the following goals: highest possible flux density at the sample; use of an existing refocusing mirror attached to the microscope; minimization of the deflection angle to allow high energies to pass; a sufficiently large deflection angle to avoid interference with existing vacuum chambers; minimum costs.

It is a feature of this kind of full-field imaging microscopes like the present one that the photon transport optics can be rather cheap and simple. They function as a condenser system and so do not need to preserve coherence for instance, as is required in scanning systems.

The arrangement chosen is shown in Fig. 1 and consists of a toroidal deflection mirror with the light incident at a grazing angle of 6°. The manipulator provides linear movement in a horizontal direction to insert or remove the mirror, as well as pitch, roll and yaw movements for alignment. The optical parameters are given in Table 1. The deflection chamber also contains a calibrated photodiode type AXUV-100† which can be inserted to measure the photon flux.

The light is brought to an intermediate focus at a diagnostic chamber, equipped with a fluorescent screen and another photodiode mounted on a vertical linear-motion feedthrough. The vertical beam profile can also be measured by monitoring the photocurrent at the microscope while scanning the photodiode holder through the beam. During alignment the pitch and roll of the deflection mirror were adjusted to position the light on the fluorescent screen and then the yaw was adjusted to obtain a horizontal line focus.

† Photodiodes supplied by International Radiation Detectors Ltd; email: ird@kaiwan.com.

The refocusing mirror attached to the microscope is toroidal and its parameters are also given in Table 1. The manipulator provides three translation axes as well as pitch and roll. No yaw adjustment is provided: the yaw was minimized by surveying into position. The light is incident on the sample at a grazing angle of 15°.

This scheme of magnification of the light spot followed by subsequent demagnification is not the ideal situation; double demagnification would be preferable but is impossible due to physical constraints. However it provides an economic means of beam transport consistent with the existing vacuum chambers.

3. Results

3.1. Optical results

The spot measured at the sample for a monochromator exit slit opening of 80 μm was slightly elliptical with an average diameter of 30 μm (Fig. 2). The major axis was expected to be horizontal but was found to be rotated by an angle of $\sim 37^\circ$ with respect to the horizontal. Calculations indicate that a yaw error of 0.3° on the refocusing mirror will cause such a rotation of the image. The photon flux density is not significantly reduced so a correction was not attempted.

A photodiode was inserted in the microscope in the sample position and the flux was measured (Table 2). The energy resolution was not measured but is theoretically between 10 meV (at 45 eV) and 70 meV (at 160 eV). This is much higher than the energy resolution of the microscope, $\sim 0.3\text{--}0.4$ eV, but cannot be degraded by further opening of the slits to increase flux density. Opening the slits simply causes the spot size at the sample to enlarge, and there is a gradient of photon energy across the spot. We are currently working on schemes to obtain better optical matching, including the use of an elliptical refocusing mirror to give stronger focusing.

In addition to the flux values under optimized conditions, a series of undulator spectra were taken at the diagnostic chamber before the final refocusing mirror (Fig. 3) for selected values of the gaps. The slit conditions were 80 and 180 μm corresponding to a larger illuminated area on the sample, and a higher flux. The flux in the microscope is lower due to reflection losses at the refocusing mirror. There may also be discrepancies as the flux in the microscope is measured with the usual grazing angle of incidence whereas in the diagnostic the beam is incident normally to the diode, and we do not have data on the angular response of the diode. These spectra are informative in any case as the individual spectra indicate the maximum range over which the photon energy range can be scanned without changing the gap. The maximum flux is indicated by the peak of each curve; at intermediate photon energies the gap can be tuned to obtain maximum flux. Experience indicates that the flux from grating 4 is generally too low to use.

The upper cut-off in energy is determined by the angles of reflection on the two mirrors and their reflectivity. Theoretically the transmission drops to 36.8% (*i.e.* $1/e$) of the maximum transmission at 180 eV. In practice we find useful transmission up to about 160 eV, depending on the photoemission cross section of the sample.

Switching the light from one branch to the other is fast and reliable as it involves inserting the deflection mirror and only a few minutes to check and fine-tune the alignment of the light in the microscope. On removal of the mirror, no re-alignment of the gas-phase branch is necessary.

3.2. Fresnel diffraction

The images shown in Fig. 4 were taken at three different photon energies. They show a triangular-shaped island, ~ 180 nm high, with a shadow cast by the light which is incident from the right at three different photon energies. Diffraction fringes parallel to the shadow edges are very noticeable, and the first maximum is clearly brighter than the intensity far from the edge. These images were taken with secondary electrons and we interpret the contrast as being entirely due to diffraction of the incident light. To check that the fringes were unrelated to other effects, such as photoelectron diffraction, an image was also taken with valence-band photoelectrons, which showed similar fringes.

Fig. 5 shows a line scan of the fringes in Fig. 4(b). They were generated by integrating the intensity parallel to the fringes over the area in which the fringes were uniform. In a first approximation the intensity can be calculated by assuming a sharp and perfectly absorbing edge, and evaluating the Kirchhoff integral (Cowley, 1995; Smith & Thompson, 1988),

$$\psi(\mathbf{x}) = (1/4\pi) \int_0^{\infty} A(r) [\exp(ikr)/r] \cos(\chi) da,$$

where ψ is the amplitude of the wave at the measuring position \mathbf{x} , r is the distance from the point \mathbf{x} to a point on the incident wave front, A is the amplitude of the incident wavefront and χ is the angle between r and the incident wavefront, and da is an element of area of the wavefront.

This yields the calculated curves in Fig. 5. Note that the fringes are uniformly spaced, in contrast to the case of diffraction from an edge viewed on a flat screen parallel to the edge and perpendicular to the light. In that case the

Table 2

Fluxes and flux densities.

Flux measured in photons s^{-1} (200 mA ring current) $^{-1}$. Flux density measured in photons s^{-1} (200 mA ring current) $^{-1} \mu m^{-2}$.

Photon energy (eV)	Flux (measured)	Flux density
135 eV	1.4×10^{13} (after exit slit)	–
135 eV	0.5×10^{13} (sample)	5.6×10^9
65 eV	1.0×10^{13} (after exit slit)	–
65 eV	0.3×10^{13} (sample)	3.3×10^9

position of the n th fringe is proportional to $n^{1/2}$, so that the fringes become closer together as the distance from the edge increases (Smith & Thompson, 1988). The linear spacing is a consequence of the viewing plane being at a large angle with respect to the incident light. For grazing angles of incidence and distances to the projection plane large compared with the wavelength of light, it can be shown that the position of the fringes have a spacing approximately equal to

$$(n\lambda \sin \alpha / \cos^2 \alpha) \{1 + [f(n, h, \alpha)]^{1/2}\} \propto n,$$

where α is the angle of incidence measured from the normal, h is the height of the island and n is the number of the fringe. f is a slowly varying function. This gives an almost linear spacing of the fringes.

The contrast, *i.e.* the difference between maximum and minimum intensity, is not reproduced by the calculation, but almost all experimental limitations, such as defocus, finite spatial and energy resolution or surface roughness, reduce the contrast.

A more precise consideration of the diffraction conditions takes account of a number of subtleties, namely the polarization of the light, the dielectric response of the surface and finite penetration of the solid. The light is p -polarized in this case; if it had been s -polarized then, in the case of a perfect conductor, the field at the surface would be zero, which shifts the fringes away from the island.

In any case, the response of the surface to the electric field implies that the near-surface field is not equal to the field far from the surface. This field at the surface can be calculated from the optical constants (Henke *et al.*, 1993) of lead and using the Fresnel reflection coefficients as in the case of photoemission (Jacobi *et al.*, 1977). At 91.2 eV the

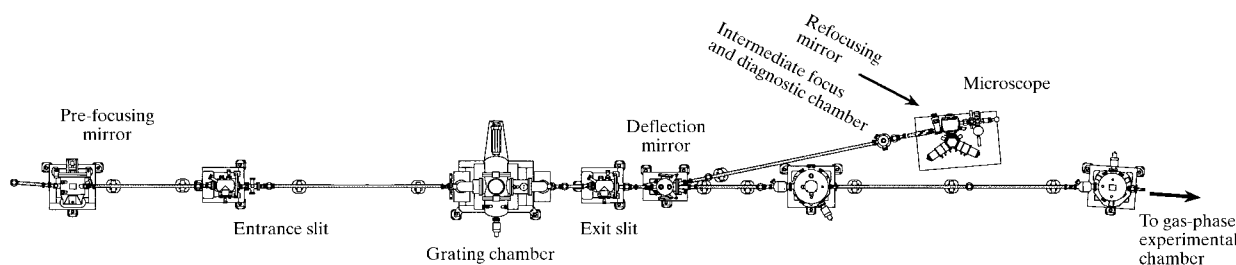


Figure 1
Optical layout of the branch beamline.

amplitude of the field at the surface is reduced. The effect was modelled by considering a field which rises from the surface to the vacuum value exponentially with distance from the surface. Small changes occurred in the intensity of the first few fringes, as well as a rigid shift of all fringes by 0.2 of one fringe spacing, or 21 nm at 91.2 eV. In the present case this corresponds to a very small error in the calculation of the height of the lead island from the position of the fringes.

The effect of finite transmission of the light through the lead island was also calculated. The attenuation length in lead varies from 3 to 6 nm in the range considered. Model calculations, which ignore refraction and phase-retardation effects, indicate a negligible displacement of the fringes. Thus, with the present photon energy and particular values of the dielectric constants, errors are negligible. However, at higher energies of several hundred eV for instance, the constants change substantially and then these effects may become significant.

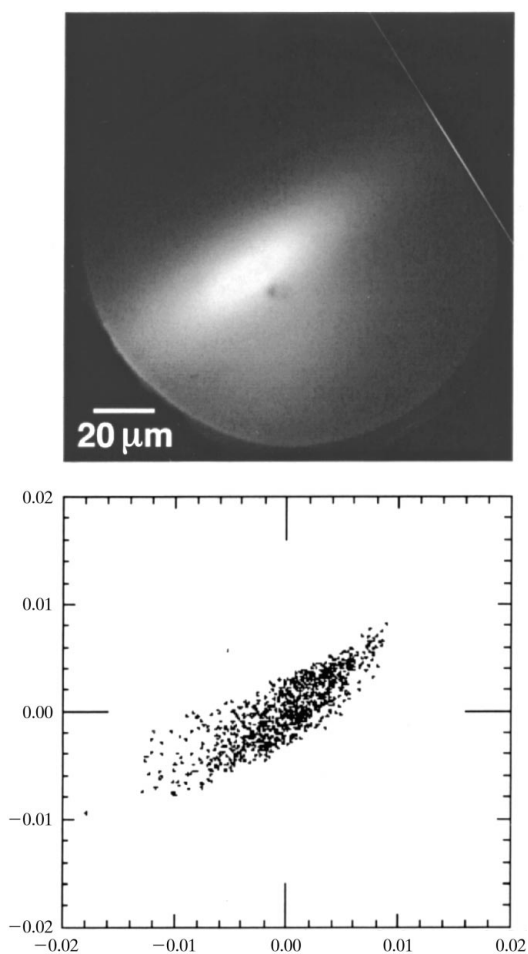


Figure 2

Image of the illuminating light spot intensity at low magnification and the calculated intensity distribution. The bottom edge of the figure is parallel to the horizontal direction in the laboratory frame. Exit slit opening: 80 μm. Average spot size: 30 μm.

These effects will be reduced for normal emission but another effect is expected for this type of island. It is very common for islands of f.c.c. metals to resemble the present form, with a (111) plane parallel to the substrate and {111} surfaces bounding it at an angle of 54.7°. Such an object will then act as a nanoscale interferometer (Fig. 6). For this geometry the fringe spacing is 7.06 times the wavelength. The effect will only be significant at energies below

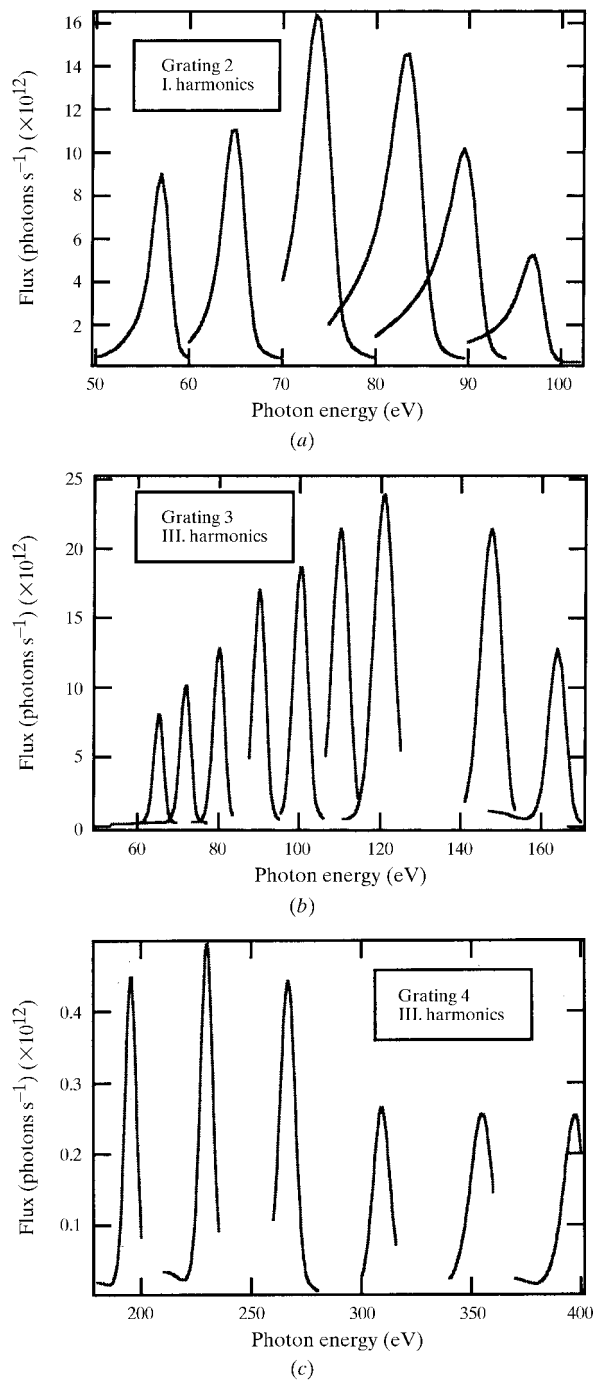


Figure 3

Series of undulator curves at selected gaps, measured at the diagnostic chamber. Slits: 80 and 180 μm. (a) grating 2, (b) grating 3, (c) grating 4.

~30–40 eV as few materials have sufficient reflectivity at higher energies.

3.3. Microspot NEXAFS

The facility to perform microspot partial-yield near-edge X-ray absorption fine-structure spectroscopy has also been developed. The total current to the fluorescent screen (with the kinetic energy set to a value in the secondary) is measured by a nanoammeter while the photon energy is scanned; this gives the NEXAFS spectrum of the field of view. An example from an Si(111) surface with a low coverage of Au and carbon is shown in Fig. 7(a). The sample can then be imaged using secondary electrons and a chosen photon energy. This is the mode of operation of most installed photoemission microscopes, but there are

two important differences in the present instrument. Firstly, the energy filter selects a narrow band of energy, minimizing chromatic aberration and increasing spatial resolution. Secondly, the electron kinetic energy can be tuned, thus tuning the surface sensitivity and/or the intensity due to density of states above the vacuum level. An example of an image is shown in Fig. 7(b).

The present system is still under development. Clearly it can already be used to perform constant final-state spectroscopy, by setting the kinetic energy to an appropriate value and scanning the photon energy. This spectroscopy is useful in band-mapping studies, for example. In future we plan to implement microspot constant initial-state spectroscopy, which is useful for scanned energy photoelectron diffraction and optimizing the choice of photon energy with respect to cross section.

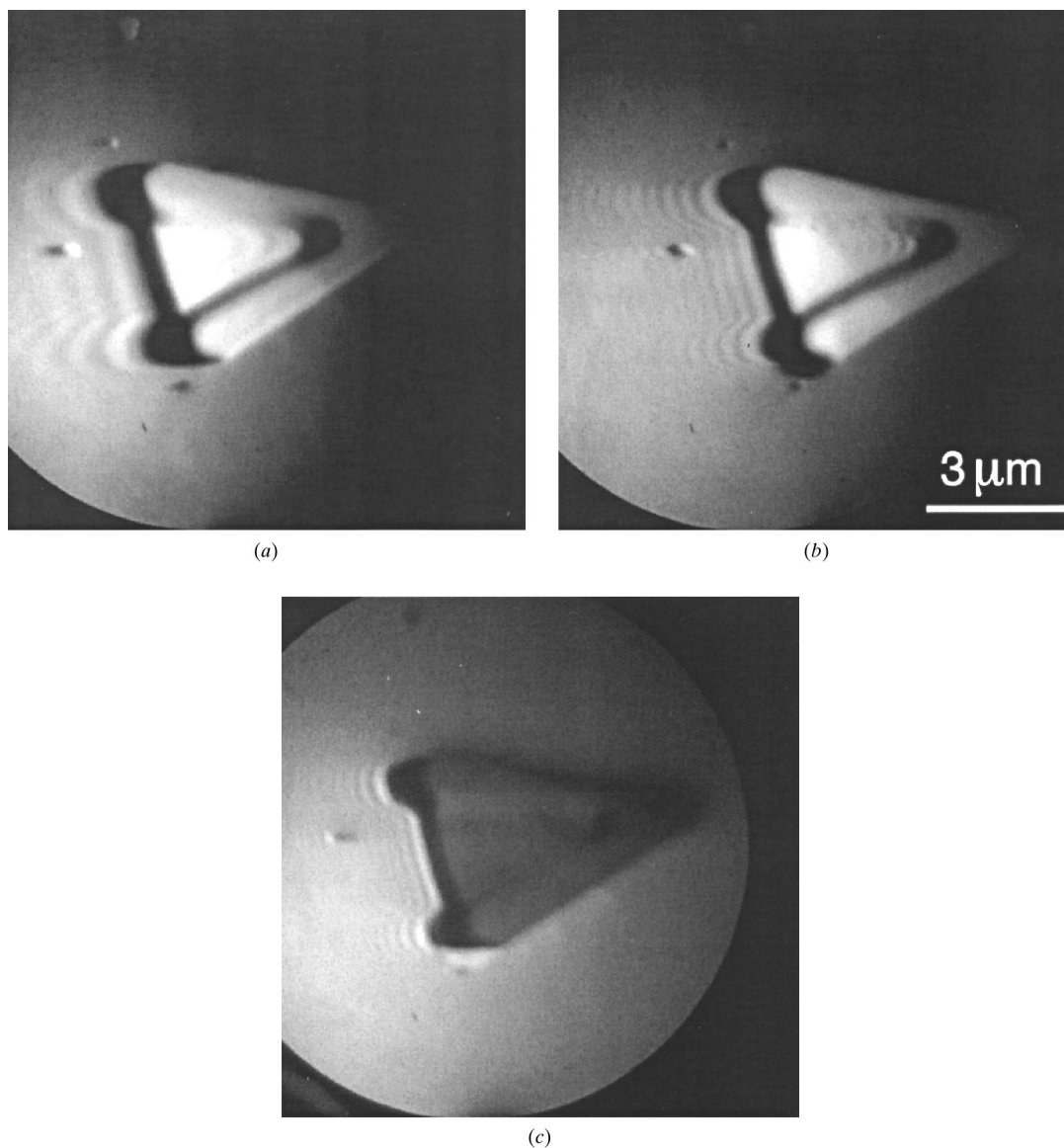


Figure 4 Lead island on Si(111). The synchrotron light is incident from the right at a grazing angle of 15° . (a) Photon energy 49.7 eV, wavelength = 24.9 nm. (b) Photon energy 91.2 eV, wavelength = 13.6 nm. (c) Photon energy 139.6 eV, wavelength = 8.9 nm.

4. Summary

The optical layout has been described for a photoemission microscopy beamline. Some of the first effects observed include Fresnel fringes which have not been reported before in photoelectron microscopy, probably due to lack of resolution or use of scanning systems, in which the effect is not evident. Illumination at off-normal incidence provides an advantage in that the height of objects on the surface can be estimated from the shadow length. On the other hand, diffraction fringes cause the region near the shadow to be no longer uniformly illuminated and therefore photoelectron emission intensity is no longer quantitatively proportional to local concentration. The fringes were useful for optimizing focus, just as they are in transmission electron microscopy. To measure accurately the height of an island by its shadow length, the dielectric response of the substrate material can be ignored at the present level of resolution. However, when higher spatial

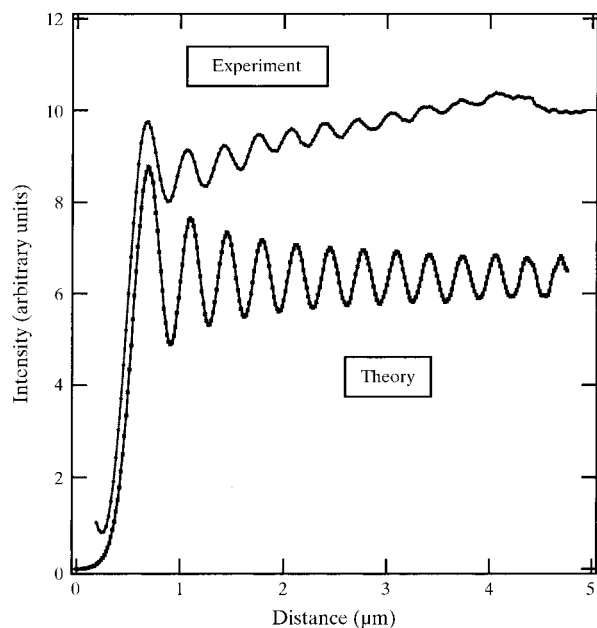


Figure 5
Line scan across the diffraction fringes of Fig. 4(b), and calculated intensity.

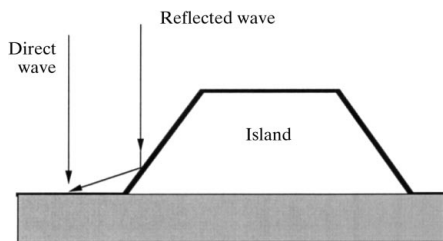


Figure 6
Schematic diagram of an island acting as a nanoscale interferometer.

resolution becomes available, this must be considered to avoid errors.

We thank J. Suchy for additional optical calculations, and G. Sostero for assistance with optical metrology. This work was supported by the Deutsche Forschungsgemeinschaft and the German Bundesministerium für Bildung und

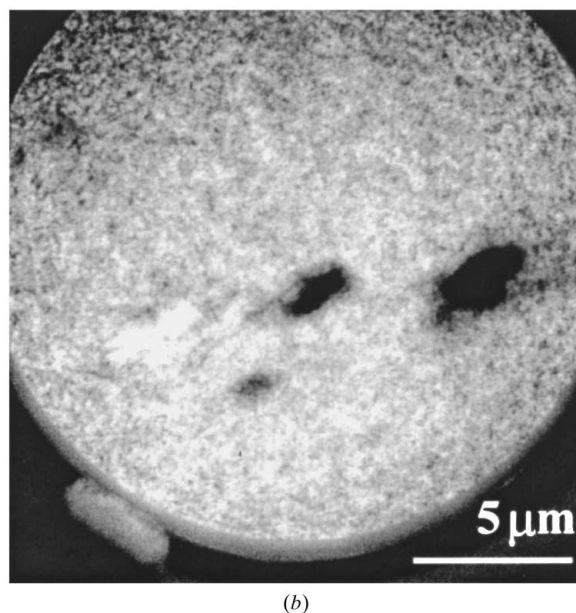
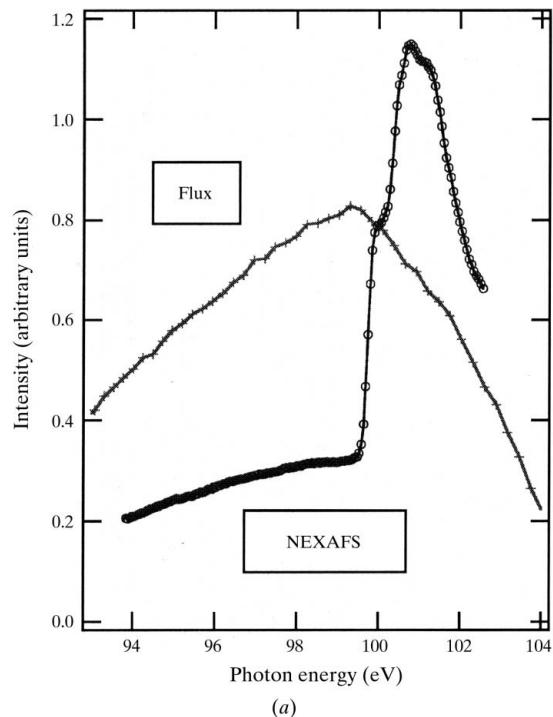


Figure 7
(a) NEXAFS spectrum of a $(\sqrt{3} \times \sqrt{3})$ Au-Si(111) surface. The curve marked 'Flux' is the photocurrent at a photodiode; the curve marked 'NEXAFS' is the integrated signal from the phosphor screen. (b) Image of the surface taken at a photon energy of 101 eV and kinetic energy of 3.7 eV. The dark areas are due to carbon contamination on the surface. The light area to the left was identified in photoemission as a gold-rich area.

Forschung (BMBF). TS acknowledges support from the EU under contract No. ERBFMBICT961749.

References

- Cowley, J. M. (1995). *Diffraction Physics*. Amsterdam: North-Holland.
- Ferrer, S., Comin, F., Fajardo, P., Santoni, A., Etgens, V., Torrelles, X. & Formoso, V. (1995). *Nucl. Instrum. Methods Phys. Res. B*, **100**, 536–539.
- Henke, B. L., Gullikson, E. M. & Davis, J. C. (1993). *Atom. Data Nucl. Data Tables*, **54**, 181–342. (www-xro.lbl.gov:80/optical_constants/.)
- Jacobi, K., Scheffler, M., Kambe, K. & Forstmann, F. (1977). *Solid State Commun.* **22**, 17–21.
- Melpignano, P., Di Fonzo, S., Bianco, A. & Jark, W. (1995). *Rev. Sci. Instrum.* **66**, 2125–2128.
- Prince, K. C., Blyth, R. R., Delaunay, R., Zitnik, M., Krempasky, J., Slezak, J., Camilloni, R., Avaldi, L., Coreno, M., Stefani, G., Furlani, C., de Simone, M. & Stranges, S. (1998). *J. Synchrotron Rad.* **5**, 565–568.
- Schmidt, Th., Heun, S., Slezak, J., Diaz, J., Prince, K. C., Lilienkamp, G. & Bauer, E. (1998). *Surf. Rev. Lett.* **5**, 1287–1296.
- Smith, F. G. & Thompson, J. H. (1998). Editors. *Optics*, 2nd ed. New York: J. Wiley & Sons.
- Veneklasen, L. H. (1991). *Ultramicroscopy*, **36**, 76–85.